Si$_7$Ti$_4$Ni$_4$ as a buffer material for Si and its electrochemical study for lithium ion batteries

CrossMark

Kyung Jae Lee [a,b], Seung-Ho Yu [a,b], Jung-Joon Kim [a,b], Dae-Hyeok Lee [a,b], Jungjin Park [a,b], Soon Sung Suh [c], Jong Soo Cho [d], Yung-Eun Sung [a,b,*]

[a] Center for Nanoparticle Research, Institute for Basic Science (IBS), Seoul 151-742, Republic of Korea
[b] School of Chemical and Biological Engineering, Seoul National University, Seoul 151-742, Republic of Korea
[c] Samsung SDI, 428-5 Gongse-dong, Giheung-gu, Kyunggi-do, Yongin 446-577, Republic of Korea
[d] MK electron, 316-2 Geumeo-ri, Pogok-myeon, Kyunggi-do, Yongin 449-810, Republic of Korea

HIGHLIGHTS

- We report a facile method for synthesis of nano-Si embedded in Si$_7$Ti$_4$Ni$_4$ complex.
- Microstructure change of Si$_7$Ti$_4$Ni$_4$ relaxes volume expansion of Si.
- Si$_7$Ti$_4$Ni$_4$ inhibits further synthesis of SEI layer.
- Discharge capacity is maintained at almost 800 mAh g^{-1} over 50 cycles.
- It retains 86% of capacity at 3200 mA g^{-1} compared to that of 400 mA g^{-1}.

ARTICLE INFO

ABSTRACT

Nano-Si embedded Si$_7$Ti$_4$Ni$_4$ is synthesized with the melt spinning method, which is facile, and applicable to mass-production. Si$_7$Ti$_4$Ni$_4$, the buffer material, is electrochemically inactive toward lithium. Nevertheless, Si$_7$Ti$_4$Ni$_4$ has good electrical conductivity, in the order of 10^5 S m^{-1}, which is more conductive than amorphous carbon that is usually used as a coating material for active material. Furthermore, the surrounding grain boundaries of Si$_7$Ti$_4$Ni$_4$ effectively relax volume expansion of Si. Therefore, it plays a critical role in maintaining the structure of electrode and the integrity of active materials. As a result, nano-Si embedded in Si$_7$Ti$_4$Ni$_4$ shows outstanding cycle performance over 50 cycles at 400 mA g^{-1}, and it maintains 86% of its specific capacity at 3200 mA g^{-1}, compared with that of 400 mA g^{-1}. This indicates that nano-Si embedded in Si$_7$Ti$_4$Ni$_4$ can be a promising anode material for lithium ion batteries.

© 2013 Elsevier B.V. All rights reserved.

1. Introduction

Lithium ion batteries (LIBs) have drawn considerable interest, due to the various possibilities of their application, such as cellular phones, laptop computers and small IT equipment. In contrast to conventional LIB, however, future LIBs will require high specific capacity and outstanding power performance. This is due to the fact that the new areas for LIBs to be applied to, such as electric vehicles and energy storage systems, require such properties. In reality, conventional electric vehicles thus far suffer from lack of inferior mileage, and slow maximum speed, in contrast to vehicles with fossil fuel. In addition, the abundance of materials is also a critical issue, as LIBs are applied to expanded areas. Therefore, it is important to find a material with high capacity and power performance that is plentiful.

To find materials which fulfill such properties, many candidates have been researched for a long time, such as metal oxide, and alloy materials [1–4]. Among these possible candidates, Si is the most promising material for future LIBs, due to its high specific capacity of around 3580 mAh g^{-1}, abundance, and low reacting voltage of around 0.2 V vs. Li/Li$^+$, which is favorable for energy density [5–8]. Nevertheless, Si presents several problems, such as low electrical conductivity, large volume change during reaction with lithium, and the resulting pulverization of active material during cycling [9–11]. In more detail, Si reacts with 3.75 Li atoms at room

temperature during lithiation, resulting in large volume expansion of around 300%. Si repeats the volume expansion and contraction during lithiation and de-lithiation, which leads to pulverization of the Si particles, finally resulting in loss of electric contact with the current collector, and so capacity fading occurs.

Many kinds of approaches have been attempted to overcome these problems, such as nano-sized structures [12–15], coatings [16–18], and matrix-buffered structures [19–21]. It was reported in many researches that nano-sized Si is more favorable to resist fracture [22,23], and coatings on Si could buffer critical volume expansion. These attempts were successful in improving cycle performances, and some products showed good performance, even at relatively high current density. These attempts, however, eventually met difficulties in real application to LIBs, due to the limitations in mass production, and low packing density of nano-materials.

In this work, nano-sized Si embedded in $Si_7Ti_4Ni_4$ (the complex is abbreviated to STN) was synthesized using the melt-spinning method (Fig. S1), which is a promising technique for mass production. This method has already been used industrially for synthesizing polymer fibers such as nylon or polyester, and promising results for synthesizing amorphous metal fibers and metal alloy fibers have recently been shown [24–26]. The synthesized STN materials were pulverized to micron-sized particles, making it beneficial to the packing density. Research into SiTiNi alloys and its application to lithium ion batteries has already been done [27–30]. These results, however, largely focused on the microstructure dependence on the Si and the Ti content [27,28], and the possibility of SiTiNi alloys being applied to lithium ion batteries [29,30]. On the other hand, in this work, we focus on the investigation of buffer material, $Si_7Ti_4Ni_4$, and in depth analysis of the electrochemical performance of STN. The intrinsic properties were measured with various analytic methods, such as transmission electron microscopy (TEM), X-ray diffraction (XRD), and 4-point probe, and the electrochemical activity of the buffer material, $Si_7Ti_4Ni_4$, toward lithium was examined with X-ray absorption near-edge structure (XANES). Furthermore, electrochemical performances of STN with various current densities were carried out, and the reasons for STN to show outstanding electrochemical performance were investigated with TEM and electrochemical impedance spectroscopy (EIS), after cycles.

2. Experimental

2.1. Preparation of materials

STN was synthesized by a melt spinning method from MK electronics. The procedure is as follows: 66 at. % Si, 17 at. % Ti and 17 at. % Ni were melted in a crucible, using an induction heating method. A thin stream of the molten metal was spun onto a rotating Cu wheel, and quenched rapidly (10^6 K s^{-1}), forming a ribbon. The as-prepared ribbon was pulverized to 8-μm average particle size by ball-milling. Then, the powders were filtered using 325 mesh (Daihan Sci., Korea), to sort out particles above 45 μm. $Si_7Ti_4Ni_4$-targeted material was synthesized using similar method: Stoichiometric amount of Si, Ti and Ni (atomic ratio of 7:4:4 respectively) were melted in a crucible by an induction heating method. The resulting molten metal was mixed well, slowly cooled in the crucible, and after cooling, the as-prepared material was pulverized by ball-milling. Nano-Si used was a commercial product form Sigma−Aldrich. Carbon coating on nano-Si was done with dopamine [31,32]. 0.2 g of nano-Si was mixed with 0.15 g of dopamine in 50 ml of Tris-buffer (pH 8.5), and stirred at 30 °C for 25 h. Then, polymer/nano-Si composite was separated by centrifugation, and washed with deionized water. The prepared composite was dried in a vacuum oven, and then carbonized at 400 °C for 2 h under Ar atmosphere. Finally, the material was heat treated at 800 °C for 3 h under Ar atmosphere.

2.2. Characterization

The composition and structure of STN were identified with XRD (Rigaku, D-MAX2500-PC) with Cu Kα radiation (λ = 1.5406 Å) at 40 kV and 200 mA, and TEM (JEOL JEM-2100F). Before the TEM measurements, the prepared material was sliced to a few hundreds of nanometers thick using a focused-ion beam (FIB), and its microstructure was observed with TEM, and selected area electron diffraction (SAED) pattern.

$Si_7Ti_4Ni_4$-targeted material with the same stoichiometric ratio as the buffer material was synthesized, and the properties, such as electrical resistivity and electrochemical activity toward lithium, were studied with a 4-point probe with pressure (LORESTA GP MCP T610), and X-ray absorption near-edge structure (XANES). Electrical resistivity of $Si_7Ti_4Ni_4$-targeted material was measured with a 4-point probe. The sample holder was filled with $Si_7Ti_4Ni_4$-targeted material powder and external pressure was applied to make a good physical connection. The intrinsic electrical resistivity was then measured. The TEM and SAED patterns were measured at the Korea Advanced Nano Fab Center (KANC), the 4-point probe measurements with pressure were performed at the Central Research Institute of Samsung SDI, and XANES was measured at the Pohang Accelerator Laboratory (PAL, 8C-line).

2.3. Cell fabrication and electrochemical measurement

82 wt. % STN, 6 wt. % Ketchen Black and 12 wt. % polyamide−imide (PAI) binder were mixed with N-methyl-2-pyrrolidone solvent, to form slurry. The prepared slurry was spread onto a copper foil, used as a current collector, using the doctor blade method. To activate the PAI binder, the as-prepared electrode was heat-treated at 350 °C under Ar atmosphere for 90 min, then vacuum-dried at 120 °C for 8 h. The prepared electrodes were transferred to an Ar-filled glove box, and cells were assembled. The electrolyte was 1.5 M LiPF$_6$ with EC/DEC/FEC (5/70/25 volume ratio, Panatech Korea), and the separator was from SK Innovation. Lithium metal was used as a counter electrode, and the cell type was 2016.

Electrochemical properties, such as the charge/discharge process with various current densities, were measured with a WBCS3000 cycler (Won-A Tech, Korea). The voltage window for electrochemical measurements was 0.01–1.5 V vs. Li/Li$^+$ (all the voltages below are vs. Li/Li$^+$). Discharge was done in a current density of 400 mA g^{-1} following a constant voltage of 0.01 V, until the current density had reached 9 mA g^{-1}, and charge was done galvanostatic with the specified constant current densities. Before the practical cycles above, formation cycles were carried out; discharge with 100 mA g^{-1} and constant voltage of 0.01 V, until the current density had reached 9 mA g^{-1}, and charge with 100 mA g^{-1}. The same process with a current density of 200 mA g^{-1} was performed.

To measure EIS, a symmetric cell was used to separate the effects from the Lithium metal side; two cells, which were cycled to the same condition, were transferred into an Ar-filled glove box, disassembled, and re-assembled into a symmetric cell. EIS was conducted with open-circuit voltage in 5 mV amplitude, and the frequency range was from 100 kHz to 50 mHz (Zahner, Germany).

3. Results and discussion

3.1. Characterization of STN

The XRD patterns of STN in Fig. 1 show that STN is composed of Si and $Si_7Ti_4Ni_4$. Sharp peaks at 2θ = 28.47, 47.34 and 56.17°, which are assigned to the (111), (220) and (311) of crystalline Si, respectively, reflect that the Si in STN is well crystallized (Si, JCPDS card
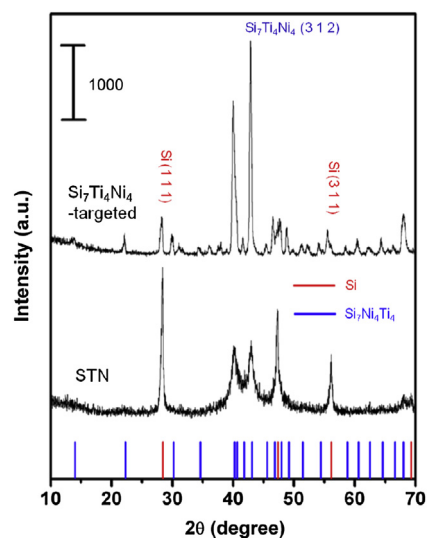
Fig. 1. XRD patterns of $Si_7Ti_4Ni_4$-targeted material and STN (JCPDS card no. 27-1402, 42-1122 for Si and $Si_7Ti_4Ni_4$, respectively).

Table 1
Electrical resistivity of $Si_7Ti_4Ni_4$-targeted material along applying external load.

	Load (kN)	Pressure (MPa)	Thick-ness (mm)	Resistance (Ω)	Electrical resistivity ($\Omega.m$)	Density (g cm^3)
1	4.00	12.73	6.00	4.052×10^{-3}	6.088×10^{-5}	3.621
2	8.00	25.46	5.80	2.225×10^{-3}	3.308×10^{-5}	3.746
3	12.00	38.20	5.66	1.595×10^{-3}	2.352×10^{-5}	3.839
4	16.00	50.93	5.56	1.276×10^{-3}	1.870×10^{-5}	3.909
5	20.00	63.66	5.46	1.083×10^{-3}	1.577×10^{-5}	3.979

The microstructure of STN can be also deduced from a phase diagram of Si, Ni, and Ti [36]. When hot molten metal, which is composed of the equal atomic percentages of Ti and Ni is cooled, the resulting metal will be separated into Si and V-phase ($Si_7Ti_4Ni_4$), and their quantity will be determined by the lever rule between Si and V-phase [37]. Therefore, the quantity of nano-Si can be adjusted from this information.

3.2. The intrinsic properties of $Si_7Ti_4Ni_4$

To investigate the properties of $Si_7Ti_4Ni_4$, $Si_7Ti_4Ni_4$-targeted material is synthesized with stoichiometric amounts of Si, Ni and Ti that is same as that of the buffer material, and its composition is checked with XRD, as in Fig. 1. There are peaks from the well crystallized $Si_7Ti_4Ni_4$ at $2\theta = 40.24$ and $43.12°$. There are, however, also peaks from Si as an impurity at $2\theta = 28.47$, 47.34 and 56.17°, unfortunately. It is difficult to make exact $Si_7Ti_4Ni_4$ composition without Si impurities because $Si_7Ti_4Ni_4$ is not a strictly stoichiometric compound, as can be seen in the phase diagram of Si, Ni and Ti [36]. In the case of $Si_7Ti_4Ni_4$-targeted material, there is enough time for $Si_7Ti_4Ni_4$ to grow to a large size, so $Si_7Ti_4Ni_4$ in the $Si_7Ti_4Ni_4$-targeted material has sharper XRD peaks, than those of the $Si_7Ti_4Ni_4$ in STN.

The electrical resistivity of $Si_7Ti_4Ni_4$-targeted material is measured by 4 point probe with the application of external load, and the results are shown in Table 1. As the external load become heavier, the electrical resistivity become lower, because of the increase in packing density, resulting in the improvement of contact between particles. The electrical resistivity of sample is proportional to volume ratio [38]. As can be seen in Fig. 1, $Si_7Ti_4Ni_4$-targeted material is composed of mostly $Si_7Ti_4Ni_4$ buffer and a small amount of nano-Si. Therefore, the majority of measured electrical resistivity can be referred to that of $Si_7Ti_4Ni_4$ buffer. In the experimental conditions, the electrical resistivity of the $Si_7Ti_4Ni_4$ is of the order of 10^{-5} Ω m. In comparison, the electrical resistivity of amorphous carbon is of the order of 10^{-4} Ω m [39]. As such, it can be expected that there may be no problems with electron

no. 27-1402). On the other hand, relatively broad peaks at $2\theta = 40.24$ and $43.12°$, which are assigned to the (501) and (312) of crystalline $Si_7Ti_4Ni_4$, mean that the $Si_7Ti_4Ni_4$ in STN has relatively small grain size. This is due to the fact that in the case of $Si_7Ti_4Ni_4$, the melt spinning method's fast cooling rate, which leaves short time for grains to grow, results in the small grain size of $Si_7Ti_4Ni_4$; on the other hand, the large latent heat of Si makes the local cooling rate in the Si side decrease, resulting in relatively larger grain size of Si than that of $Si_7Ti_4Ni_4$.

The microstructure of STN is shown in Fig. 2. Approximately 100-nm-sized Si particles are dispersed in the $Si_7Ti_4Ni_4$, and some agglomerates of these Si particles are found. According to Liu et al. [33], nano-Si, below 150 nm in size, can stand tensile stresses throughout the lithium insertion, leading to improved resistance against pulverization. Therefore, it is expected that the inherent nano-sized Si in STN will show good cycle performances. Furthermore, the facile synthesis of nano-Si structure in STN can be an outstanding advantage. The spotted SAED pattern of Si and the ring-shaped SAED pattern of $Si_7Ti_4Ni_4$ in Fig. 2(b) reflect well crystallized Si and polycrystallized $Si_7Ti_4Ni_4$, which shows the same result in Fig. 1. Its small grain size and the resulting numerous grain boundaries are beneficial to the lithium ion movement, and results in good cell performance in high current density [34,35].
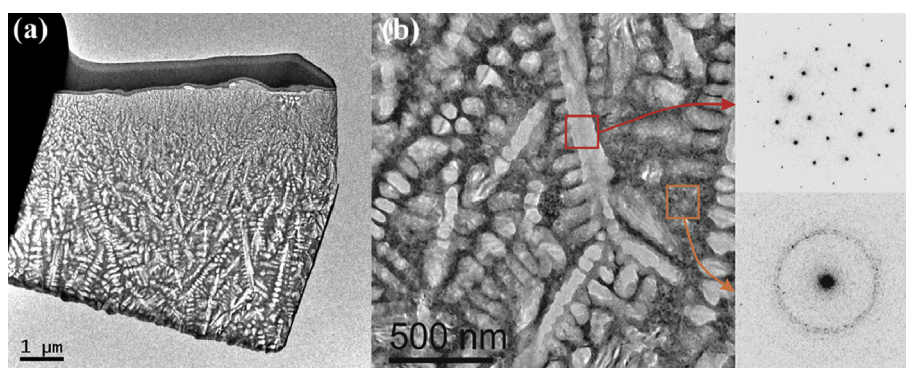

Fig. 2. TEM images: (a) cross-sectional view of raw STN and (b) high-magnification cross-sectional view of STN. The inset shows selected area electron diffraction (SAED) patterns of Si and $Si_7Ti_4Ni_4$ parts, respectively.

conduction through $Si_7Ti_4Ni_4$. Furthermore, $Si_7Ti_4Ni_4$ is an inorganic framework, which is more rigid than organic frameworks such as amorphous carbon, so it should work more effectively to prevent volume expansion, and consequently have better cycle retention. The superior properties of inorganic framework throughout the cycles will be mentioned in Subsection 3.4.

The activity of $Si_7Ti_4Ni_4$ toward lithium is investigated, and the results are shown in Fig. 3. The $Si_7Ti_4Ni_4$-targeted material shows relatively negligible specific capacity of around 30 mAh g^{-1}. Its charge/discharge profile is similar to that of a capacitor, except for the existence of reacting voltage around 0.4 V and 0.01 V, which can be explained by the formation of solid electrolyte interphase (SEI), and the reaction of lithium with Si impurities in the $Si_7Ti_4Ni_4$-targeted material [40,41].

The XANES of the Ti K edge and the Ni K edge of the $Si_7Ti_4Ni_4$-targeted material are measured as the cycle progresses, to confirm the electrochemical activity of $Si_7Ti_4Ni_4$ toward lithium in Fig. 4. The measurements are executed 1) before the cycle, and after 2) discharging to 0.05 V, 3) discharging to 0.01 V, 4) discharging to 0.01 V, and holding at 0.01 V until current density reaches 9 mA g^{-1}, and then 5) charging to 0.2 V, 6) charging to 1.5 V. There are no significant changes in the onset and edge of the normalized absorbance profiles, which means that the oxidation states of Ti and Ni do not change as the cycle progresses. If the $Si_7Ti_4Ni_4$ reacts with the lithium, then the oxidation state of Ti or Ni may change, due to the electrons inserted as the reaction proceeds [42,43].

Therefore, from the specific capacity of the $Si_7Ti_4Ni_4$-targeted material and XANES data, it can be concluded that $Si_7Ti_4Ni_4$ is inactive toward lithium, and the STN has a structure of active nano-Si surrounded by inactive, also electrically conductive, $Si_7Ti_4Ni_4$ phase.

3.3. Electrochemical performance of STN

The charge/discharge profile and its differential capacity profile (dQ/dV) profiles of STN in response to cycling are shown in Fig. 5. According to Dahn et al. [44], Si shows two reacting voltages, which depend on lithium reaction environments, such as the lithium co-ordination number of the reacting site; one is for the case in which lithium surrounds Si, and the other is for the case in which lithium surrounds lithium that had previously entered. Similarly, there are two cathodic peaks at 0.3 and 0.1 V in the discharging process in Fig. 5(b), which reflects that Si in STN reacts with lithium. Also, dQ/dV profile for STN is typical of reaction between Si and lithium [45], which reveals that the Si in STN reacts with lithium.

The cycle performance and power performance of STN with different current densities are shown in Fig. 6. STN shows almost constant specific capacity, of around 800 mAh g^{-1} over 50 cycles, at 400 mA g^{-1}. In the case of nano-Si as control group, however, it shows poor cycle retention throughout the cycles, in the same current density and slurry composition. Though Carbon coated nano-Si shows better performance than nano-Si, due to its improved electrical conductivity and structural stability, it also
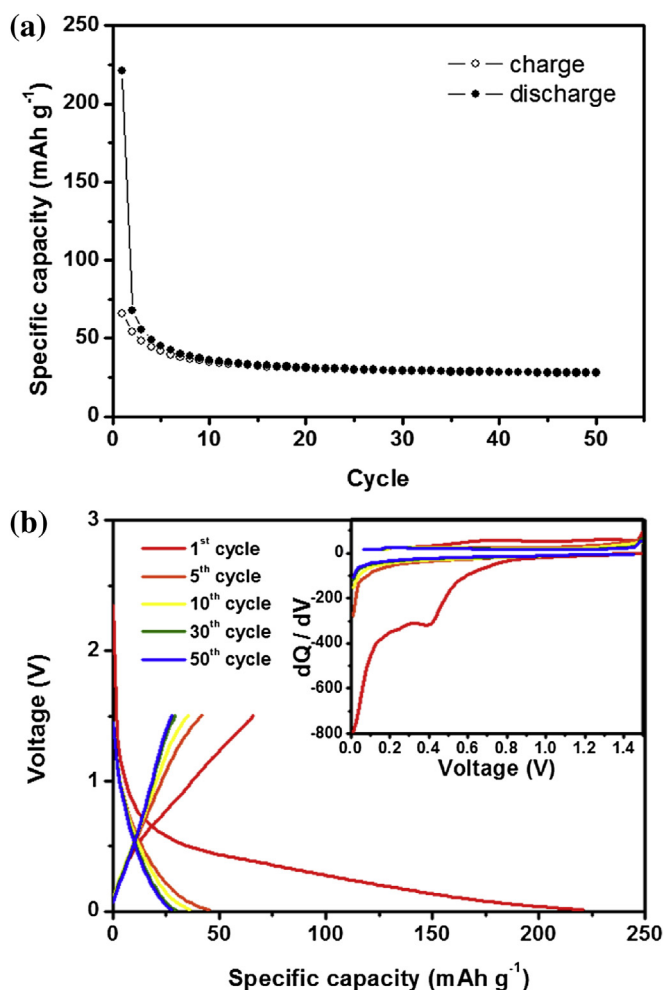

Fig. 3. (a) Cycle performance and (b) charge/discharge profile for $Si_7Ti_4Ni_4$-targeted material at the current density of 100 mA g^{-1}. The inset is a profile of dQ/dV.

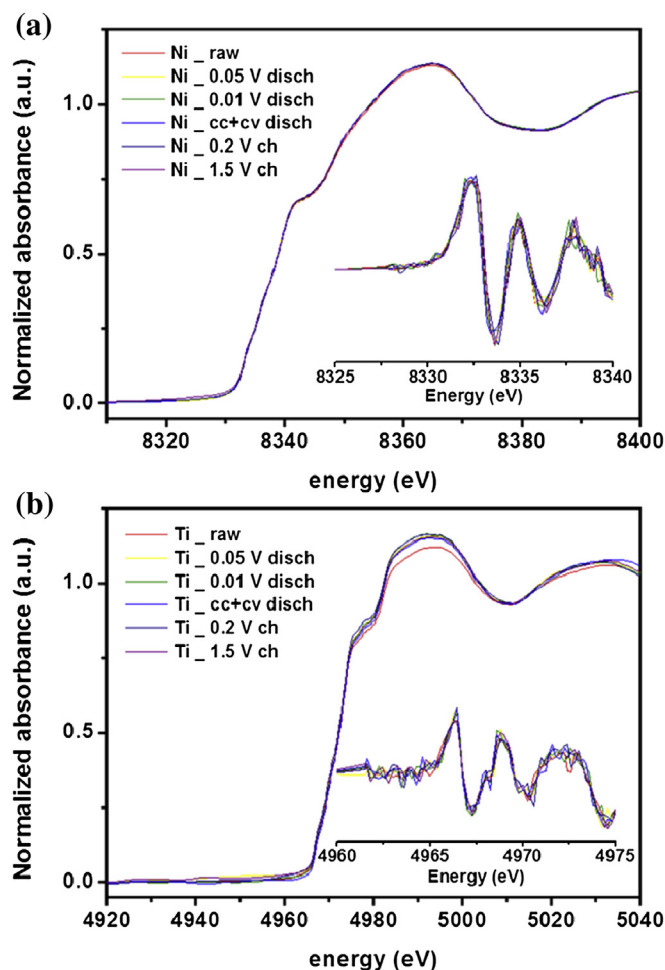**Fig. 4.** X-ray absorption near-edge structure (XANES) of $Si_7Ti_4Ni_4$-targeted material along the cycle: (a) Ni K edge, (b) Ti K edge. The inset is differential absorbance.
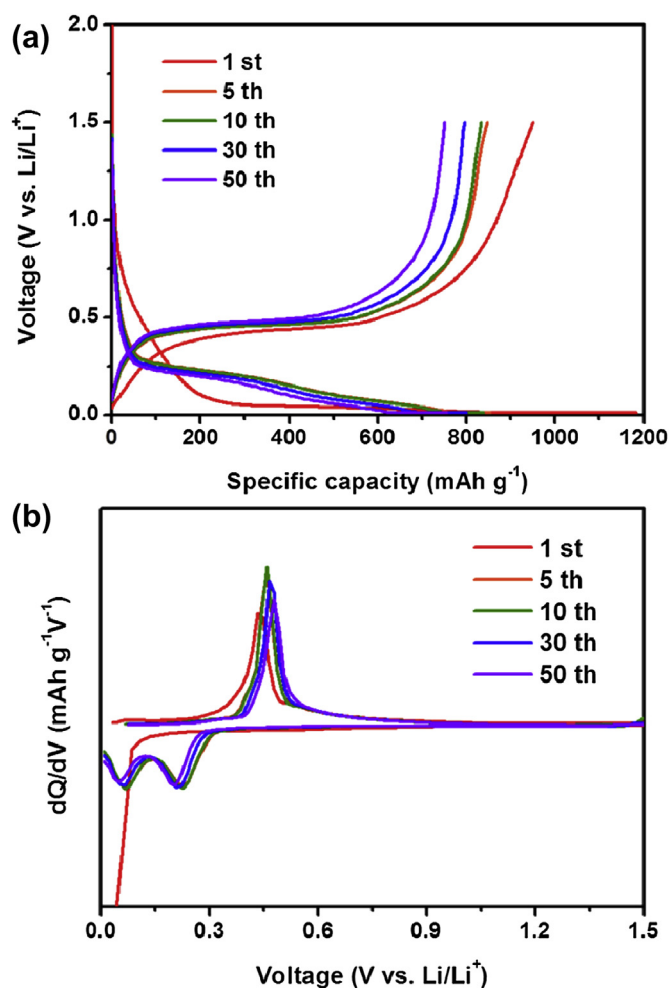
Fig. 5. (a) Charge/discharge profile and (b) dQ/dV profile of STN at current density of 400 mA g^{-1}.

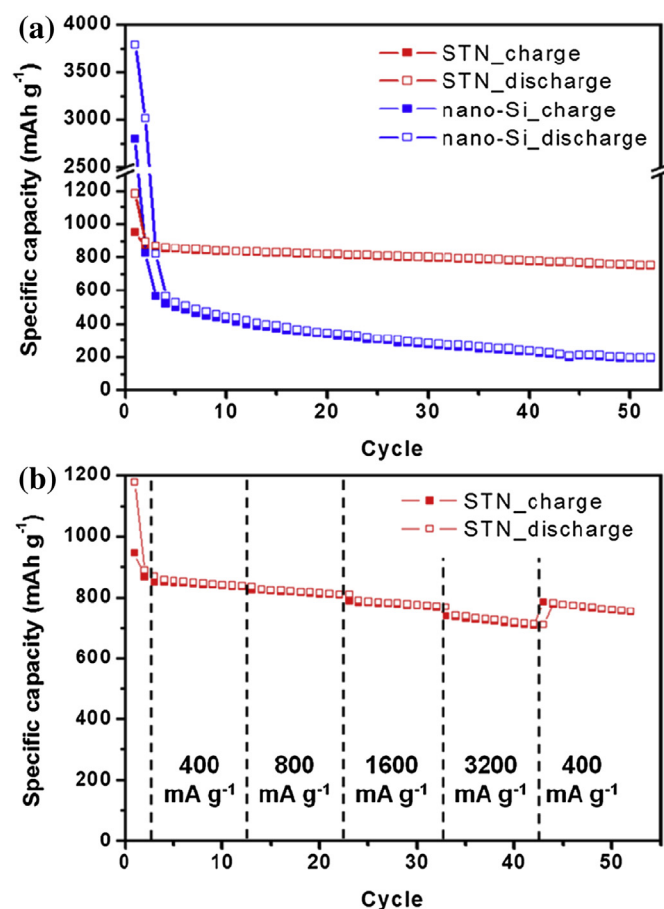**Fig. 6.** Electrochemical performance of STN. (a) Cycle properties of STN and nano-Si, as a control group, with current density of 400 mA g^{-1} and (b) power property of STN in various current densities.

suffers from sudden capacity decay within the first 10 cycles as shown in Fig. S3. In general, sudden capacity fading for active materials with large volume change, such as Si and Sn, is due to the electrical disconnection that occurs between the active materials and the current collector. This disconnection arises due to pulverization of the electrode due to repeated volume expansion and contraction. This phenomenon is observed in the case of nano-Si and carbon coated nano-Si. On the other hand, STN shows relatively stable cycle performance, which reflects that STN endures volume expansion effectively, which in turn, maintains the original structure of the electrode, thus resulting in good electrical connection between the active materials and the current collector, throughout the cycles (Fig. S4). In addition, STN has better coulombic efficiency in the first formation cycle than nano-Si due to its smaller surface area, which is critical issue in commercialization of active materials. Furthermore, STN shows good power performance: it maintains 86% of the specific capacity at 3200 mA g^{-1}, compared with that of 400 mA g^{-1}, and recovers its specific capacity, when current density returns to 400 mA g^{-1}. Therefore, it is confirmed that STN could stand high current density, and lithium can diffuse effectively through $Si_7Ti_4Ni_4$.

The theoretical specific capacity of STN is around 990 mAh g^{-1}. The STN is composed of 66 at. % of Si, 17 at. % of Ti and 17 at. % of Ni. Therefore, it can be roughly estimated that 29.75 at. % of Si is in the $Si_7Ti_4Ni_4$ phase, which is inactive, and only 36.25 at. % of Si exhibits capacity, so the theoretical specific capacity of STN is 990 mAh g^{-1},

assuming that one Si reacts with 3.75 Li atoms. A possible reason for the relatively small specific capacity of STN is the nonstoichiometry of $Si_7Ti_4Ni_4$. In the Si/Ti/Ni phase diagram, the $Si_7Ti_4Ni_4$ phase is not a point, but a small region, which means that the component ratio of the $Si_7Ti_4Ni_4$ could be changed, to some extent. The amount of Si in STN is determined by the lever rule between pure Si and Si rich-$Si_7Ti_4Ni_4$ ($Si_{7+\delta}Ti_4Ni_4$); therefore, there is a small amount of reactive Si, compared with that of Si calculated from the exact ratio of $Si_7Ti_4Ni_4$. Nevertheless, when this capacity, around 800 mA g^{-1}, is converted by the mass of active nano-Si, it shows a high specific capacity, of around 3000 mAh g$^{-1}_{of\ active\ Si}$. Moreover, STN materials with a higher specific capacity can be made from smaller amount of Ni and Ti. For example, the STN composed of 68 at. % of Si, 16 at. % of Ti and 16 at. % of Ni will have 40 at. % of active Si and 28 at. % of inactive Si in $Si_7Ti_4Ni_4$. Such a compound has a larger amount of active Si than that of the STN composed of 66 at. % of Si, 17 at. % of Ti and 17 at. % of Ni, mentioned above. When there is higher amount of active Si, however, it means there is smaller amount of $Si_7Ti_4Ni_4$, which is vital toward relieving the stresses induced by volume expansion of Si. Therefore, there is a tradeoff between specific capacity and cyclability.

3.4. Gradual change with cycle

TEM of STN after the formation cycle is shown in Fig. 7. After the formation cycle, STN retains its nano-Si embedded in the $Si_7Ti_4Ni_4$ structure. While, nano-Si in the STN expands its volume toward the grain boundaries of $Si_7Ti_4Ni_4$, where contractive stress can be
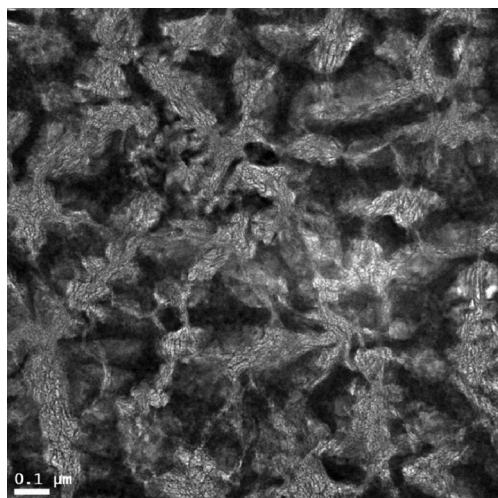
Fig. 7. TEM image of STN after the formation cycle. The bright side is Si, and the dark side is $Si_7Ti_4Ni_4$.

released, and the integrity of STN is maintained. It is the same principle when hollow Si expands: it resolves contractive stress by expanding inward, where there is free volume [45,46]. In addition, expansion of nano-Si induces network of nano-Si to be integrated into the grain boundaries of $Si_7Ti_4Ni_4$, resulting in an increase of contact surface between lithium and Si as shown in Fig. 7. Furthermore, the nano-Si becomes smaller, resulting in an improved property against pulverization.

Electrochemical impedance Nyquist plots at open circuit voltage of 0.1 V after 5 cycles and 15 cycles, and their fitting results are shown in Fig. 8. The equivalent circuit that is used for fitting and the fitted data, R_{sei} and R_{ct}, are presented in inset of Fig. 8. R_{sei} is the resistance, related to lithium ion diffusion through the solid electrolyte interphase (SEI) region, and R_{ct} is the resistance of faradaic reactions, in this case, those between lithium and Si. As the fitting results show, R_{sei} and R_{ct} have no meaningful change throughout the cycles. This throws a sidelight on the fact that there is no significant SEI layer thickness change throughout the cycles [47], and it means that the buffer material, $Si_7Ti_4Ni_4$, deals with the volume expansion effectively. Therefore, even though $Si_7Ti_4Ni_4$ is a buffer material, which is inactive toward lithium, resulting in disadvantage with respect to gravimetric specific capacity, its advantages,

such as its role in relaxing volume expansion and maintaining integrity of active material and electrode, far exceeds the disadvantages and is beneficial to overall performance.

4. Conclusions

The STN consisting of nano-sized Si embedded in inactive $Si_7Ti_4Ni_4$ phase is synthesized with the melt spinning method. This method is promising for easy mass production, making this material adequate for real application to LIBs. Moreover, inherent nanosized Si is beneficial for enduring volume expansion, and the resulting pulverization. The $Si_7Ti_4Ni_4$, buffer material is inactive toward lithium, which is unfavorable in the aspect of gravimetric specific capacity. Nevertheless, $Si_7Ti_4Ni_4$ has good electrical conductivity, making it an excellent coating material. In addition, the surrounding grain boundaries of $Si_7Ti_4Ni_4$ effectively absorb contractive stress induced by volume expansion of Si, resulting in maintaining its structural integrity throughout the cycles. The microstructural change throughout the cycle is beneficial for increased contact area between the Si and lithium, and the ability to endure volume expansion, due to the smaller size of Si. This results in good cycle performance, even in a high current density of 3200 mA g^{-1}. Such a stable cycle performance and the outstanding power performance of STN make it a good candidate for anode materials in the next generation LIBs.

Appendix A. Supplementary data

Supplementary data related to this article can be found at http://dx.doi.org/10.1016/j.jpowsour.2013.08.033.
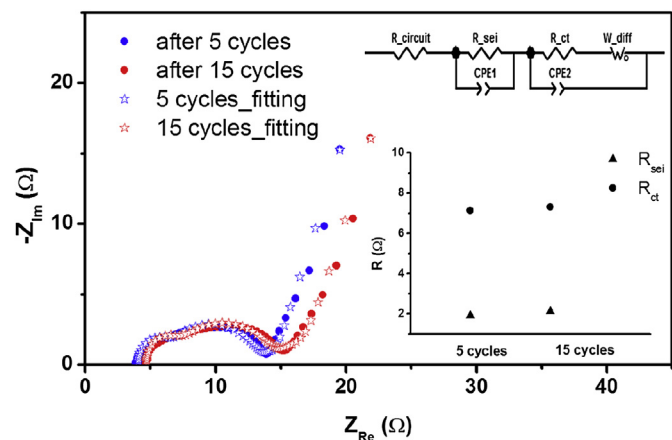

Fig. 8. Electrochemical impedance Nyquist plots at open circuit voltage of 0.1 V after 5 cycles and 15 cycles. Equivalent circuit used for fitting and fitted results, R_{ct} and R_{sei}, are in the inset.

References

[1] P. Poizot, S. Laruelle, S. Grugeon, L. Dupont, J.-M. Tarascon, Nature 407 (2000) 496–499.
[2] S. Baek, S.-H. Yu, S.-K. Park, A. Pucci, C. Marichy, D.-C. Lee, Y.-E. Sung, Y. Piao, N. Pinna, RSC Adv. 1 (2011) 1687–1690.
[3] B. Liu, Z.P. Guo, G. Du, Y. Nuli, M.F. Hassan, D. Jia, J. Power Sources 195 (2010) 5382–5386.
[4] N. Pereira, M. Balasubramanian, L. Dupont, J. McBreen, L.C. Klein, G.G. Amatucci, J. Electrochem. Soc. 150 (2003) A1118–A1128.
[5] C.K. Chan, H.L. Peng, G. Liu, K. McIlwrath, X.F. Zhang, R.A. Huggins, Y. Cui, Nat. Nanotechnol. 3 (2008) 31–35.
[6] A. Magasinski, P. Dixon, B. Hertzberg, A. Kvit, J. Ayala, G. Yushin, Nat. Mater. 9 (2010) 353–358.
[7] Y. Yao, K. Huo, L. Hu, N. Liu, J.J. Cha, M.T. McDowell, P.K. Chu, Y. Cui, ACS Nano 5 (2011) 8346–8351.
[8] T.H. Hwang, Y.M. Lee, B.-S. Kong, J.-S. Seo, J.W. Choi, Nano Lett. 12 (2012) 802–807.
[9] R.A. Huggins, J. Power Sources 81–82 (1999) 13–19.
[10] J. Graetz, C.C. Ahn, R. Yazami, B. Fultz, Electrochem. Solid-state Lett. 6 (2003) A194–A197.
[11] J.P. Maranchi, A.F. Hepp, P.N. Kumta, Electrochem. Solid-state Lett. 6 (2003) A198–A201.
[12] L.-F. Cui, R. Ruffo, C.K. Chan, H. Peng, Y. Cui, Nano Lett. 9 (2009) 491–495.
[13] R. Teki, R. Krishnan, T.C. Parker, T.-M. Lu, P.N. Kumta, N. Koratkar, Small 5 (2009) 2236–2242.
[14] M. Holzapfel, H. Buqa, L.J. Hardwick, M. Hahn, A. Wursig, W. Scheifele, P. Novak, R. Kotz, C. Veit, F.-M. Petrat, Electrochim. Acta 52 (2006) 973–978.
[15] X.H. Liu, L.Q. Zhang, L. Zhong, Y. Liu, H. Zheng, J.W. Wang, J.-H. Cho, S.A. Dayeh, S.T. Picraux, J.P. Sullivan, S.X. Mao, Z.Z. Ye, J.Y. Huang, Nano Lett. 11 (2011) 2251–2258.
[16] H.-Y. Lee, S.-M. Lee, Electrochem. Commun. 6 (2004) 465–469.
[17] W. Wang, P.N. Kumta, ACS Nano 4 (2010) 2233–2241.

[18] S.H. Ng, J. Wang, D. Wexler, S.Y. Chew, H.K. Liu, J. Phys. Chem. C 111 (2007) 11131–11138.
[19] I.-S. Kim, P.N. Kumta, G.E. Blomgren, Electrochem. Solid-state Lett. 3 (2000) 493–496.
[20] O. Mao, R.L. Turner, I.A. Courtney, B.D. Fredericksen, M.I. Buckett, L.J. Krause, J.R. Dahn, Electrochem. Solid-state Lett. 2 (1999) 3–5.
[21] Y. Nuli, B. Wang, J. Yang, X. Yuan, Z. Ma, J. Power Sources 153 (2006) 371–374.
[22] H. Kim, M. Seo, M.H. Park, J. Cho, Angew. Chem. Int. Ed. 49 (2010) 1710–1716.
[23] U. Kasavajjula, C. Wang, A.J. Appleby, J. Power Sources 163 (2007) 1003–1039.
[24] R. Mishima, H. Miyamura, T. Sakai, N. Kuriyama, H. Ishikawa, I. Uehara, J. Alloys Compd. 192 (1993) 176–178.
[25] T. Saito, M. Itakura, J. Alloys Compd. 572 (2013) 124–128.
[26] Y.H. Zhang, B.W. Li, H.P. Ren, S.H. Guo, D.L. Zhao, X.L. Wang, Int. J. Hydrogen Energy 35 (2010) 2040–2047.
[27] S.-S. Suh, W.Y. Yoon, C.-G. Lee, S.-U. Kwon, J.-H. Kim, Y. Matulevich, Y.-U. Kim, Y. Park, C.-U. Jeong, Y.-Y. Chan, S.-H. Kang, J. Electrochem. Soc. 160 (2013) A751–A755.
[28] J.J. Song, H.J. Kwon, D.K. Ahn, Y.Y. Chu, J.S. Cho, J.T. Moon, W.-W. Park, K.Y. Sohn, J. Nanosci. Nanotechnol. 13 (2013) 3413–3416.
[29] S.-B. Son, S.C. Kim, C.S. Kang, T.A. Yersak, Y.-C. Kim, C.-G. Lee, S.-H. Moon, J.S. Cho, J.-T. Moon, K.H. Oh, S.-H. Lee, Adv. Energy Mater. 2 (2012) 1226–1231.
[30] H. Jung, Y.U. Kim, M.-S. Sung, Y. Hwa, G. Jeong, G.-B. Kim, H.-J. Sohn, J. Mater. Chem. 21 (2011) 11213–11216.
[31] R. Liu, S.M. Mahurin, C. Li, R.R. Unocic, J.C. Idrobo, H. Gao, S.J. Pennycook, S. Dai, Angew. Chem. Int. Ed. 50 (2011) 6799–6802.
[32] C. Lei, F. Han, D. Li, W.-C. Li, Q. Sun, X.-Q. Zhang, A.-H. Lu, Nanoscale 5 (2013) 1168–1175.
[33] X.H. Liu, L. Zhong, S. Huang, S.X. Mao, T. Zhu, J.Y. Huang, ACS Nano 6 (2012) 1522–1531.
[34] J.C. Fisher, J. Appl. Phys. 22 (1951) 74–77.
[35] M. Park, X. Zhang, M. Chung, G.B. Less, A.M. Sastry, J. Power Sources 195 (2010) 7904–7929.
[36] X. Hu, G. Chen, C. Ion, K. Ni, J. Phase Equilib. 20 (1999) 508–514.
[37] D.R. Gaskell, Introduction to the Thermodynamics of Materials, fifth ed., Taylor & Francis, New York, 2008.
[38] S.O. Kasap, Principles of Electronic Materials and Devices, third ed., McGraw-Hill, Singapore, 2006.
[39] R.A. Serway, Principles of Physics, second ed., Saunders College Pub, Fort Worth, Texas, 1998.
[40] J.S. Yeo, T.H. Park, M.H. Seo, J. Miyawaki, I. Mochida, S.H. Yoon, Electrochim. Acta 77 (2012) 111–120.
[41] A.J. Bard, L.R. Faulkner, Electrochemical Methods: Fundamentals and Applications, second ed., Wiley, New York, 2001.
[42] A.V. Chadwick, S.L.P. Savin, R. Alcantara, D.F. Lisbona, P. Lavela, G.F. Ortiz, J.L. Tirado, ChemPhysChem 7 (2006) 1086–1091.
[43] M.J. Aragon, B. Leon, C.P. Vicente, J.L. Tirado, A.V. Chadwick, A. Berko, S.Y. Beh, Chem. Mater. 21 (2009) 1834–1840.
[44] J. Li, A. Smith, R.J. Sanderson, T.D. Hatchard, R.A. Dunlap, J.R. Dahn, J. Electrochem. Soc. 156 (2009) A283–A288.
[45] Y. Yao, M.T. MacDowell, I. Ryu, H. Wu, N. Liu, L. Hu, W.D. Nix, Y. Cui, Nano Lett. 11 (2011) 2949–2954.
[46] N. Liu, H. Wu, M.T. McDowell, Y. Yao, C. Wang, Y. Cui, Nano Lett. 12 (2012) 3315–3321.
[47] H. Wu, G. Chan, J.W. Choi, I. Ryu, Y. Yao, M.T. McDowell, S.W. Lee, A. Jackson, Y. Yang, L. Hu, Y. Cui, Nat. Nanotechnol. 7 (2012) 310–315.